Band alignment and electrocatalytic activity at the p-n La0.88Sr0.12FeO3/SrTiO3(001) heterojunction

Wang, L.; Du, Y.; Chang, L.; Stoerzinger, K. A.; Bowden, M. E.; Wang, J.; Chambers, S. A.

2018

Wang, L., Du, Y., Chang, L., Stoerzinger, K. A., Bowden, M. E., Wang, J., & Chambers, S. A. (2018). Band alignment and electrocatalytic activity at the p-n La0.88Sr0.12FeO3/SrTiO3(001) heterojunction. Applied Physics Letters, 112(26), 261601-. doi:10.1063/1.5030897

https://hdl.handle.net/10356/89761

https://doi.org/10.1063/1.5030897

Band alignment and electrocatalytic activity at the *p-n* $La_{0.88}Sr_{0.12}FeO_3$/$SrTiO_3$(001) heterojunction

L. Wang,[1] Y. Du,[1,a)] L. Chang,[2] K. A. Stoerzinger,[1] M. E. Bowden,[3] J. Wang,[2] and S. A. Chambers[1,a)]

[1]*Physical and Computational Sciences Directorate, Pacific Northwest National Laboratory, 902 Battelle Blvd., Richland, Washington 99352, USA*

[2]*School of Materials Science and Engineering, Nanyang Technological University, Singapore 639798, Singapore*

[3]*Environmental Molecular Sciences Laboratory, Pacific Northwest National Laboratory, Richland, Washington 99352, USA*

(Received 26 March 2018; accepted 19 May 2018; published online 25 June 2018)

Ferrite perovskites have exhibited promising *p*-type conductivity and oxygen evolution reaction (OER) activity. In this work, we investigate heteroepitaxial *p-n* junctions formed by $La_{0.88}Sr_{0.12}FeO_3$ and *n*-$SrTiO_3$(001). Sr substitution for La in $LaFeO_3$ is shown to be effective for introducing p-type conductivity, lowering the optical bandgap, and enhancing electrocatalytic OER. A staggered, type-II band alignment with a large built-in potential within the LSFO forms due to the polar interface. This electronic structure facilitates charge transfer across the *p-n* junction and accounts for the strongly thickness-dependent extent of OER we observe. *Published by AIP Publishing.*
https://doi.org/10.1063/1.5030897

Hydrogen generation via photocatalytic water splitting is currently of significant interest because of its potential for low cost, clean energy production. The development of highly stable, visible-light-active photocatalytic materials is an important step in the advancement of solar hydrogen production.[1] The complex oxide solid solutions $La_{1-x}Sr_xFeO_3$ (LSFO) are of particular interest because their low band gaps maximize light absorption across the visible portion of the solar spectrum.[2–5] One end member, $LaFeO_3$ (LFO), is a wide band gap ($E_g = 2.1$ eV) antiferromagnetic insulator with a high Néel temperature ($T_N = 738$ K).[6] The other end member, $SrFeO_3$ (SFO), is a helical antiferromagnetic metal with $T_N = 134$ K.[7] Hole doping by partial substitution of Sr^{2+} for La^{3+} reduces the gap, enhances visible light absorption at lower photon energies, and results in a change in the Fe electron configuration and the formal charge from $3d^5$ (Fe^{3+}) to $3d^4$ to (Fe^{4+}).[3] In $LaFeO_3$, the top portion of the valence band consists of strongly hybridized Fe 3d and O 2p orbitals. The holes introduced in stoichiometric LSFO by Sr doping fall just above the Fermi level and have mixed Fe 3d and O 2p character,[8] similar to $La_{1-x}Sr_xCrO_3$,[9,10] leading to p-type conductivity. On the other hand, the high energy cost required to remove a 3d electron from Fe^{3+} can cause the system to compensate by creating O vacancies which stabilize Fe^{3+}. The extent to which this compensation occurs depends on the synthesis and processing conditions. Without considering the vacancies, the competition between these two processes results in significant variations in material properties depending on the details of sample preparation.[11–13]

Heterojunction formation is an effective means of separating photogenerated carriers. *n*-type $SrNb_xTi_{1-x}O_3$ (Nb:STO) has been widely used in *p-n* heterojunctions with other complex oxides.[14–17] Looking first at the end member LFO, a recent study of ultrathin LFO films grown on Nb:STO reveals that small changes in the LFO layer thickness can alter the nature of the interface, resulting in significant effects on photogenerated carrier separation across the interface.[18] Based on LFO/Nb:STO(001) heterojunctions prepared by pulsed laser deposition (PLD) with an LFO target, Nakamura *et al.*[19] reported a reversal in the orientation of the LFO polarization as the STO termination was changed from TiO_2 to SrO. Sign changes in both the short-circuit photocurrent and the rectifying polarity were observed. Likewise, Nakamura *et al.*[20] also found that the direction of visible-light photoconductivity at zero bias was dependent on the interface polarity in LFO/Nb:STO(001) heterojunctions prepared in the same way. In contrast, Comes and Chambers[21] found that LFO films grown by oxygen plasma assisted molecular beam epitaxy (OPA-MBE) with separately shuttered La and Fe beams resulted in negligible differences in valence band offsets (VBO) and potential gradients for the two interface polarities. The subsequent scanning transmission electron microscopy and electron energy loss spectroscopy (STEM/EELS) investigation by the same group revealed that the SrO monolayer deposited on Nb:STO to create the *p*-type interface was consumed during the shuttered MBE growth of LFO.[22] Looking next at LSFO solid solutions, it has been reported based on current-voltage (*I–V*) and capacitance-voltage (*C–V*) measurements that the Fermi level in LSFO shifts downward in energy with increasing Sr doping level.[11,23] Several earlier papers have shown that oxygen vacancies play an important role in perovskite oxide heterostructures, in general,[24–28] and can lead to resistive switching, which is characterized by hysteretic *I–V* behavior.[17,29] Yamamoto *et al.*[11,23] reported that hysteretic behavior is observed in some diodes for x in the range $0.4 \leq x \leq 0.8$, with the percentage of diodes showing such behavior increasing with x. In a different study, no hysteretic behavior was observed in LSFO/Nb:STO heterojunctions for $x = 0.2$ and 0.3.[11]

a)Authors to whom correspondence should be addressed: yingge.du@pnnl.gov and scott.chambers@pnnl.gov

Herein, we describe the deposition and the electronic properties of epitaxial $La_{1-x}Sr_xFeO_3$/Nb:STO *p–n* heterojunctions for x = 0.12. This value of x was chosen because it is sufficiently high to dope enough holes into LFO to yield conductivity. This x value is also close to 0.125, a convenient value for *ab initio* modelling using supercells with one of the eight A-site cations being occupied by Sr. We prepared $La_{0.88}Sr_{0.12}FeO_3$ films with thicknesses ranging from 3 to 35 unit cells (u.c.) by means of OPA-MBE and a 75 u.c. film grown by off-axis PLD (OA-PLD). Our substrates were 0.7 wt. % Nb:STO(001) chemically prepared with the TiO_2 termination. The electronic properties were determined using *in situ* x-ray photoelectron spectroscopy (XPS) as well as *ex situ* in-plane and vertical transport. Optical absorption was characterized using *ex situ* spectroscopic ellipsometry. Electrochemical activity was monitored via oxygen evolution in an *in situ* electrochemical cell. (See supplementary material for details.)

We show in Fig. 1 the Fe 2*p*, O 1*s*, Ti 2*p*, Sr 3*d* and La 4*d* core-level XPS data for three thin-film heterostructures of OPA-MBE-grown LSFO on Nb:STO(001). The Fe 2*p* line shapes are complex in that they contain contributions from angular momentum coupled multiplets, shake-up features, and the presence of some (formally) Fe^{4+} resulting from Sr doping.[30] The La 4*d* spectra contain multiplet and shake-up fine structures as well, but they are not affected by a change in valence. However, these spectra exhibit different overall peak widths for 3, 5 and 9 u.c. as a result of built-in potentials. The Fe 2*p* and La 4*d* binding energies decrease monotonically with increasing thickness as a result of these built-in potentials within the films. The O 1*s* and Sr 3*d* lineshapes show clear thickness dependences because O and Sr are present on both sides of the interface and their binding energies are determined in part by potential gradients in the LSFO, which change with thickness. The Sr 3*d* spectra can be fit using two pairs of spin-orbit doublets. The more intense doublets with higher binding energies (green) are assigned to Sr^{2+} in the STO substrates, whereas the weaker doublets (orange) originate from Sr in the LSFO films. The binding energy differences across the interface (ΔE_b) result from the band discontinuity at the interface and the built-in potentials

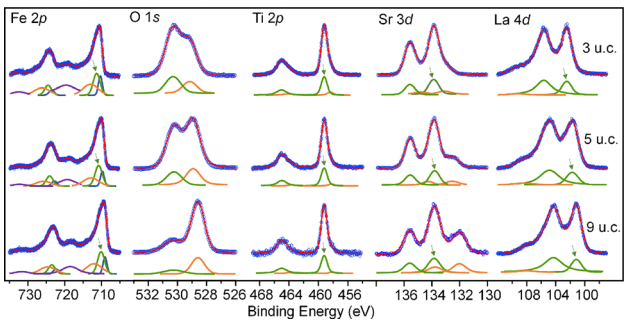

FIG. 1. Fe 2*p*, O 1*s*, Ti 2*p*, Sr 3*d* and La 4*d* photoelectron spectra of $La_{0.88}Sr_{0.12}FeO_3$/Nb:STO heterojunctions. The peak set used to fit the Fe 2*p* spectra does not represent a unique or theoretically rigorous solution, but was chosen solely to obtain a good fit and isolate a single feature (marked with a vertical arrow) for band offset determination. The fitting parameters were kept constant for all thicknesses. Likewise, the features in the Ti 2*p*, Sr 3*d* and La 4*d* spectral fits used for band offset determination are marked with arrows.

in the LSFO films. The increase in ΔE_b with film thickness indicates the sign of the built-in potential. A similar trend is seen in the O 1*s* spectra. The Ti $2p_{3/2}$ spectra can also be fit using two Voigt functions separated by ~0.8 eV. The higher binding energy peak (green) at ~459.2 eV is assigned to Ti^{4+} signals from Nb:STO. The weak peak (orange) at ~458.4 eV is assigned to outdiffused Ti in the LSFO films. The binding energy of outdiffused Ti is different from that of structural Ti^{4+} in STO because of different electrostatic potentials in the LSFO, as described in more detail below. We rule out the weak peak being due to Ti^{3+} in Nb:STO because the binding energy difference between Ti^{3+} and Ti^{4+} in *n*-STO is typically 1.5–2 eV.[31] Ti outdiffusion has also been observed in $La_{1-x}Sr_xCrO_3$/Nb:STO and $Pr_{0.64}Ca_{0.36}MnO_3$/Nb:STO.[16,32]

Using these core-level binding energies, we determined the valence band offsets (VBO, ΔE_V) using the method originally developed for Group IV and Group III–V semiconductor heterojunctions by Kraut *et al.*[33] We employ the binding energies of the Sr $3d_{5/2}$, Ti $2p_{3/2}$, Fe $2p_{3/2}$ and La $4d_{5/2}$ features marked with arrows in Fig. 1 and extract four VBO values for each heterojunction by taking pairs of core levels, with one from the substrate and one from the film. This analysis results in a consistent set of VBO values for each heterojunction, as seen in supplementary material, Table S1. The VBO for the 3 u.c. LSFO/STO heterojunction is 1.8(1) eV. This value is slightly larger than that for LFO/Nb:STO.[18,21] The VBO *apparently* increases sharply to 2.5(1) eV at 5 u.c. and then rises more modestly to 2.9(1) eV at 9 u.c. The apparent increase in VBO with film thickness is an artifact of the built-in potentials within the LSFO, which have the effect of broadening the La *4d* spectra. The top of the LSFO VB approaches the Fermi level at higher thicknesses because of hole doping (supplementary material, Fig. S3), which does not occur in LFO/Nb:STO.[18,21]

In order to estimate the built-in potentials, the broadening of the La 4*d* spectra for 3, 5 and 9 u.c. was modelled as shown in Fig. 2. The best models result when using potential drops of 50 and 300 meV/u.c. for the 3 and 5 u.c. films, respectively. The 9 u.c. film was modelled using 200 meV/u.c. for the first 4 u.c. (near the interface) and 100 meV/u.c for the second 5 u.c. (near the surface). Strictly speaking, the VBO should be determined using the La $4d_{5/2}$ binding energy for the LSFO u.c. *directly* at the interface, in order to eliminate the error incurred by using binding energies that averaged over all layers in the presence of the built-in

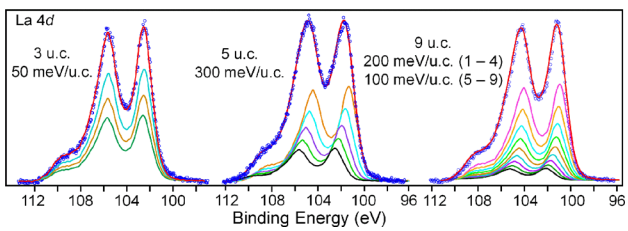

FIG. 2. La 4*d* spectra (open circles) and simulations (red curves) made by assigning the spectrum of the near-flat-band 35 u.c. film to each layer in the thin-film heterojunctions. The individual spectra were then summed after attenuating to account for depth below the surface and systematically shifted in energy, using the energy shift(s) between consecutive layers as the sole fitting parameter. The spectra of the individual layers are shown in each case.

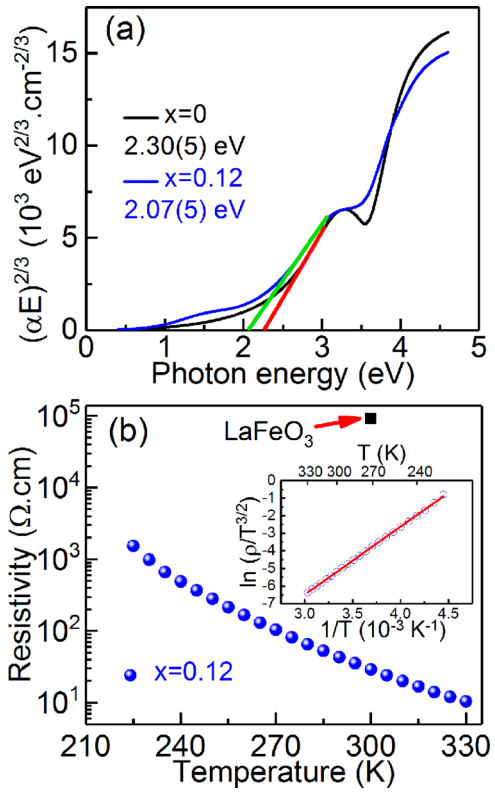

FIG. 3. (a) Spectroscopic ellipsometry measurements for a 35 u.c. LSFO film (blue and green) and a 25 u.c. $LaFeO_3$ film (black and red). (b) Temperature dependence of resistivity for a 35 u.c. LSFO film grown on undoped STO. The room-temperature resistivity of a 25 u.c. $LaFeO_3$ film is represented by the solid square. The inset shows the fit of resistivity data to a polaron conduction model.

potential. Doing so leads to VBOs of ~1.6(1) eV for the 3 and 5 u.c. films and ~1.9(2) eV for the 9 u.c. film.

The associated conduction band offsets (CBO, ΔE_C) can be determined if the band gap for LSFO is known. To this end, spectroscopic ellipsometry was used to determine the band gaps of thick films of LSFO (35 u.c.) and LFO (25 u.c.). The resulting values, taken from Tauc plots in Fig. 3(a), are 2.07(5) eV and 2.30(5) eV for LSFO and LFO, respectively. Here, the inter-band optical transitions were modelled as direct, dipole-forbidden excitations.[34] The linear region of the quantities $(\alpha E)^{2/3}$ (where α is the absorption coefficient and E is the photon energy) was extrapolated to the photon energy axis. The introduction of holes from Sr doping not only decreases the band gap of LSFO, but also leads to an increase in conductivity. Figure 3(b) shows the resistivity (ρ) versus temperature (T) for a 35 u.c. LSFO film grown on undoped STO, with a non-adiabatic polaron conduction plot [$\ln(\rho/T^{3/2})$ versus T^{-1}] shown in the inset. Sr doping causes the room-temperature resistivity of LSFO to drop by three orders of magnitude relative to epitaxial LFO. The slope of the fit in the inset yields a hole hopping activation energy (E_A) of ~0.34 eV, with consistent E_A values of 0.30–0.35 eV for $La_{1-x}Sr_xFeO_3$ with $x < 0.45$ reported elsewhere.[35]

Based on these results, we construct the energy diagram shown in Fig. 4(a). The built-in potential within the LSFO facilitates the separation of photogenerated excitons, sweeping electrons into the Nb:STO bulk and holes to the LSFO surface where they could drive water oxidation. Moreover, the large ΔE_V value creates a high barrier for holes drifting from LSFO to STO and effectively reduces electron−hole recombination at the surface which would further improve the water splitting efficiency. Figure 4(b) shows the vertical *I–V* characteristics of a 75 u.c. LSFO/Nb:STO *p–n* heterojunction. The diode shows good rectifying characteristics, with a rectifying ratio of ~40 at ±1.5 V. As seen in Fig. 4(b), the *I–V* curves do not change with the voltage sweep direction, revealing an inconsequential concentration of oxygen vacancies. As seen in the energy diagram in Fig. 4(a), ΔE_C is much smaller than ΔE_V. Thus, electrons should be the dominant carriers under forward bias. The current of the *p–n* heterojunction under low forward bias can be described by the thermionic emission model as[36]

$$I(V) = SA^*T^2 \exp\left(\frac{-\phi_B}{k_BT}\right)\left(\exp\left(\frac{eV}{nk_BT}\right) - 1\right), \quad (1)$$

where S is the junction area (~4.9×10^{-9} m^{-2}), A^* is the effective Richardson constant (~300 A cm^{-2} K^{-2}, assuming an effective mass of 3.3 m_0 for LSFO[4]), ϕ_B is the barrier height, T is the temperature, k_B is the Boltzmann constant, e is the electron charge, V is the applied voltage, and n is the ideality factor. Fitting the forward current to Eq. (1) yields a barrier height ϕ_B of ~0.67 eV and an ideality factor n of ~2.7. The ϕ_B value from *I-V* is very close to ΔE_C from XPS (0.6 ± 0.1 eV). Larger ideality factors have also been observed in other *p–n* junctions and were attributed to the

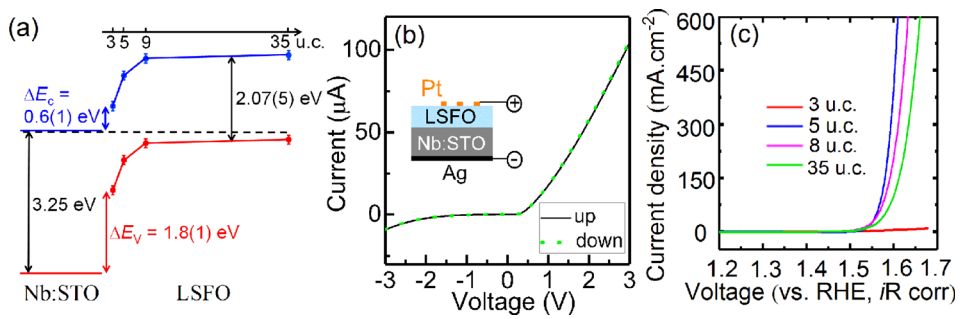

FIG. 4. (a) Energy level diagram derived from the analysis of XPS core-level and valence band spectra. The VBO (red) and CBO (blue) values are determined from the values shown in Table S1. (b) *I–V* characteristics of a 75 u.c. LSFO/Nb:STO *p-n* heterojunction measured at room temperature. The inset shows the schematic of the device measurement. (c) Cyclic voltammetry curves for the OER at a scan rate of 10 mV/s in O_2-saturated 0.1 M KOH for LSFO/Nb:STO *p-n* junctions, showing the current per LSFO surface area versus the applied voltage on the RHE scale, corrected for electrolyte resistance.

presence of interfacial states and coupled defect-driven recombination.[16,37,38]

Finally, we investigated the electrocatalytic behavior of *p*-LSFO/*n*-STO(001) by monitoring the oxygen evolution reaction (OER) for the series of films grown by OPA-MBE [Fig. 4(c)]. The applied voltage was referenced to the reversible hydrogen electrode (RHE), where the thermodynamic potential of water oxidation occurs at 1.23 V vs. RHE. The 3 u.c. LSFO/STO heterojunction exhibits negligible OER activity, possibly due to the large gap between the O 2*p* band and the Fermi level at this thickness. Similar behavior has been observed for thin LFO[18] and was thought to arise from interfacial band bending. The out-diffused Ti in LSFO, as detected by XPS, may preferentially bond with Sr dopants and lead to more Fe^{3+}. Electron transfer from Nb:STO to LSFO near the interface would nominally reduce Fe^{4+} to Fe^{3+},[39] while Fe^{4+} is more active for OER.[40] For 5 u.c. LSFO, the OER activity increases dramatically, exceeding that of undoped LFO[18] and intermediate to that of $La_{0.75}Ca_{0.25}FeO_3$ and $La_{0.5}Ca_{0.5}FeO_3$.[40] With increasing film thickness, the activity decreases slightly, potentially influenced by the impedance of hole transport to the surface and the changing energetics of the film surface/electrolyte junction. The threshold voltage for OER is ~1.5 V. The more positive potential required to drive the reaction reflects an "overpotential" stemming from kinetic losses. An in-depth investigation of the OER activity of thicker films under wavelength-selected illumination is in progress.

In summary, we have investigated the electronic structure and properties at the interface of *p*-type LSFO and *n*-STO. A large valence band offset and a substantial built-in potential within the LSFO are expected to enhance photocatalytic activity for solar water splitting and can explain the enhanced OER activity relative to that of pure LFO on *n*-STO.

See supplementary materials for details on film growth and characterization and valence band offset calculation.

This research was supported by the U.S. Department of Energy (DOE), Office of Basic Energy Sciences, Division of Materials Science and Engineering under Award No. 10122. L.C. and J.W. acknowledge financial support from the Ministry of Education, Singapore under Grant No. MOE2013-T2-1-052 and MOE2014-T2-1-099. Support for OER measurements was provided to K.A.S. by the Linus Pauling Distinguished Post-doctoral Fellowship at Pacific Northwest National Laboratory (PNNL LDRD 69319). The authors would like to thank Mark Scafetta and Tiffany Kaspar for many insightful discussions. A portion of the work was performed at the W. R. Wiley Environmental Molecular Sciences Laboratory, a DOE User Facility sponsored by the Office of Biological and Environmental Research. PNNL is a multi-program national laboratory operated for DOE by Battelle.

[1]C.-H. Liao, C.-W. Huang, and J. Wu, Catalysts **2**(4), 490 (2012).
[2]K. Parida, K. Reddy, S. Martha, D. Das, and N. Biswal, Int. J. Hydrogen Energy **35**(22), 12161 (2010).
[3]M. D. Scafetta, Y. Xie, M. Torres, J. Spanier, and S. May, Appl. Phys. Lett. **102**(8), 081904 (2013).
[4]G. T. Pan, S. Chong, K.-L. Pan, M.-B. Chang, T. C.-K. Yang, and P. Shukla, Clean Technol. Environ. Policy **19**(5), 1557 (2017).
[5]J. Yang, R. Hu, W. Meng, and Y. Du, ChemComm **52**(12), 2620 (2016).
[6]T. Arima, Y. Tokura, and J. B. Torrance, Phys. Rev. B **48**(23), 17006 (1993).
[7]S. Ishiwata, M. Tokunaga, Y. Kaneko, D. Okuyama, Y. Tokunaga, S. Wakimoto, K. Kakurai, T. Arima, Y. Taguchi, and Y. Tokura, Phys. Rev. B **84**(5), 054427 (2011).
[8]A. M. Ritzmann, A. B. Muñoz-García, M. Pavone, J. A. Keith, and E. A. Carter, Chem. Mater. **25**(15), 3011–3019 (2013).
[9]K. H. Zhang, Y. Du, P. V. Sushko, M. E. Bowden, V. Shutthanandan, S. Sallis, L. F. Piper, and S. A. Chambers, Phys. Rev. B **91**(15), 155129 (2015).
[10]K. H. Zhang, Y. Du, A. Papadogianni, O. Bierwagen, S. Sallis, L. F. Piper, M. E. Bowden, V. Shutthanandan, P. V. Sushko, and S. A. Chambers, Adv. Mater. **27**(35), 5191 (2015).
[11]A. Sawa, A. Yamamoto, H. Yamada, T. Fujii, M. Kawasaki, J. Matsuno, and Y. Tokura, Appl. Phys. Lett. **90**(25), 252102 (2007).
[12]Y. Xie, M. D. Scafetta, R. J. Sichel-Tissot, E. J. Moon, R. C. Devlin, H. Wu, A. L. Krick, and S. J. May, Adv. Mater. **26**(9), 1434 (2014).
[13]A. Khare, D. Shin, T. S. Yoo, M. Kim, T. D. Kang, J. Lee, S. Roh, I. H. Jung, J. Hwang, S. W. Kim, T. W. Noh, H. Ohta, and W. S. Choi, Adv. Mater. **29**(37), 1606566 (2017).
[14]E. Lesne, N. Reyren, D. Doennig, R. Mattana, H. Jaffrès, V. Cros, F. Petroff, F. Choueikani, P. Ohresser, R. Pentcheva, A. Barthélémy, and M. Bibes, Nat. Commun. **5**, 4291 (2014).
[15]X. R. Wang, C. J. Li, W. Lü, T. Paudel, D. Leusink, M. Hoek, N. Poccia, A. Vailionis, T. Venkatesan, J. Coey, E. Y. Tsymbal, Ariando, and H. Hilgenkamp, Science **349**, 716–719 (2015).
[16]Y. Du, C. Li, K. H. Zhang, M. E. McBriarty, S. R. Spurgeon, H. S. Mehta, D. Wu, and S. A. Chambers, Appl. Phys. Lett. **111**(6), 063501 (2017).
[17]L. Wang, Q. Zhang, L. Chang, L. You, X. He, K. Jin, L. Gu, H. Guo, C. Ge, Y. Feng, and J. Wang, Adv. Electron. Mater. **3**(10), 1700321 (2017).
[18]K. J. May, D. P. Fenning, T. Ming, W. T. Hong, D. Lee, K. A. Stoerzinger, M. D. Biegalski, A. M. Kolpak, and Y. Shao-Horn, J. Phys. Chem. Lett. **6**(6), 977 (2015).
[19]M. Nakamura, F. Kagawa, T. Tanigaki, H. Park, T. Matsuda, D. Shindo, Y. Tokura, and M. Kawasaki, Phys. Rev. Lett. **116**(15), 156801 (2016).
[20]K. Nakamura, H. Mashiko, K. Yoshimatsu, and A. Ohtomo, Appl. Phys. Lett. **108**, 211605 (2016).
[21]R. Comes and S. Chambers, Phys. Rev. Lett. **117**(22), 226802 (2016).
[22]S. R. Spurgeon, P. V. Sushko, S. A. Chambers, and R. B. Comes, Phys. Rev. Mater. **1**(6), 063401 (2017).
[23]A. Yamamoto, A. Sawa, H. Akoh, M. Kawasaki, and Y. Tokura, Appl. Phys. Lett. **90**(11), 112104 (2007).
[24]I. Justicia, P. Ordejón, G. Canto, J. L. Mozos, J. Fraxedas, G. A. Battiston, R. Gerbasi, and A. Figueras, Adv. Mater. **14**(19), 1399 (2002).
[25]D. A. Muller, N. Nakagawa, A. Ohtomo, J. L. Grazul, and H. Y. Hwang, Nature **430**(7000), 657 (2004).
[26]J. Jeong, N. Aetukuri, T. Graf, T. D. Schladt, M. G. Samant, and S. S. P. Parkin, Science **339**(6126), 1402 (2013).
[27]R. Mishra, Y.-M. Kim, J. Salafranca, S. K. Kim, S. H. Chang, A. Bhattacharya, D. D. Fong, S. J. Pennycook, S. T. Pantelides, and A. Y. Borisevich, Nano Lett. **14**(5), 2694 (2014).
[28]L. Wang, S. Dash, L. Chang, L. You, Y. Feng, X. He, K. Jin, Y. Zhou, H. G. Ong, P. Ren, S. Wang, L. Chen, and J. Wang, ACS Appl. Mater. Interfaces **8**(15), 9769 (2016).
[29]P. Sharma, S. Ryu, J. D. Burton, T. R. Paudel, C. W. Bark, Z. Huang, E. Y. Tsymbal, G. Catalan, C. B. Eom, and A. Gruverman, Nano Lett. **15**(5), 3547 (2015).
[30]T. Droubay and S. A. Chambers, Phys. Rev. B **64**, 205414 (2001).
[31]M. S. J. Marshall, D. T. Newell, D. J. Payne, R. G. Egdell, and M. R. Castell, Phys. Rev. B **83**(3), 035410 (2011).
[32]G. Saucke, J. Norpoth, C. Jooss, D. Su, and Y. Zhu, Phys. Rev. B **85**(16), 165315 (2012).
[33]E. A. Kraut, R. W. Grant, J. R. Waldrop, and S. P. Kowalczyk, Phys. Rev. Lett. **44**(24), 1620 (1980).
[34]M. D. Scafetta, A. M. Cordi, J. M. Rondinelli, and S. J. May, J. Phys. Condens. Matter **26**(50), 505502 (2014).
[35]Y. J. Xie, M. D. Scafetta, E. J. Moon, A. L. Krick, R. J. Sichel-Tissot, and S. J. May, Appl. Phys. Lett. **105**(6), 062110 (2014).
[36]S. M. Sze and K. K. Ng, *Physics of Semiconductor Devices* (John Wiley & Sons, 2006).

[37]K. Zheng, J. L. Zhao, X. W. Sun, V. Q. Vinh, K. S. Leck, R. Zhao, Y. G. Yeo, L. T. Law, and K. L. Teo, Appl. Phys. Lett. **101**(14), 143110 (2012).
[38]K. H. Zhang, R. Wu, F. Tang, W. Li, F. E. Oropeza, L. Qiao, V. K. Lazarov, Y. Du, D. J. Payne, J. L. MacManus-Driscoll, and M. G. Blamire, ACS Appl. Mater. Interfaces **9**(31), 26549–26555 (2017).
[39]K. A. Stoerzinger, M. Risch, J. Suntivich, W. M. Lü, J. Zhou, M. D. Biegalski, H. M. Christen, T. Venkatesan, and Y. Shao-Horn, Energy Environ. Sci. **6**(5), 1582 (2013).
[40]J. Suntivich, K. J. May, H. A. Gasteiger, J. B. Goodenough, and Y. Shao-Horn, Science **334**(6061), 1383 (2011).